1-bit memory using one electron: Parametric oscillations in a Penning trap

C. H. Tseng,* D. Enzer,† and G. Gabrielse

Department of Physics, Harvard University, Cambridge, Massachusetts 02138

F. L. Walls

National Institute of Standards and Technology, Boulder, Colorado 80303

The parametric oscillation of a single trapped electron is studied and used to measure enhanced spontaneous emission. Hysteresis in this motion provides a 1-bit memory to store information about excitations made with the electron ''in the dark.'' The time dependence and stability criteria for the parametric excitation are examined. The cyclotron motions for one and two electrons are also studied. [S1050-2947(99)01303-7]

PACS number(s): 32.80.Pj

I. INTRODUCTION

An electron in a Penning trap is typically observed by driving its axial motion along the magnetic field direction with a driving force that is nearly resonant [1]. Instead, we modulate the trapping potential and thereby parametrically drive the electron's axial motion at approximately twice its resonant frequency. The magnitude and phase of the response are separately measured and compared to theoretical expectations [2], along with resonance line shapes, bistability, hysteresis, and the time required to excite to a steady state. These studies [3] are done in extremely high vacuum, in an apparatus virtually identical to that used to establish a pressure less than 5×10^{-17} Torr [4], thereby avoiding the collisions which dominated an earlier observation [5]. Parametric resonance is used to measure rapid, enhanced spontaneous emission for electron cyclotron motion in a trap cavity, at a rate too fast to have been measured previously [6]. The bistability and hysteresis in parametric resonance are used to measure the cyclotron resonance frequency with a resolution of 1 part in 10^9, a resolution which corresponds to the relativistic shift in the cyclotron frequency caused by increasing the cyclotron quantum number by 1. This resolution is attained while the electron is ''in the dark'' insofar as all nearly resonant drives (other than the cyclotron drive) and detectors are turned off, to avoid significantly increasing the electron's amplitude. Bistability and hysteresis in the parametric oscillator are used as a 1-bit memory to record whether or not a cyclotron excitation occurs. ''In the dark'' detection should make it possible to increase the accuracy of tests of quantum electrodynamics which are already the most accurate comparison of a physics experiment [7] and theory [8].

II. PARAMETRIC RESONANCE AND STEADY STATE

One electron is stored at the center of the Penning trap represented in Fig. 1. Two end-cap electrodes, above and below, and a ring electrode are shaped along the hyperbolic contours which are the equipotentials of the desired electrostatic quadrupole potential. An ''orthogonalized'' geometry [9] makes it possible to improve the shape of the trapping potential (by adjusting the potential on the asymptotic compensation electrodes) without changing the electron's oscillation frequencies. A 5.3 T magnetic field is directed along the vertical axis. An electron in this Penning trap undergoes the familiar motions [1] illustrated in Fig. 1. Throughout this paper we shall assume that the slow magnetron motion [at frequency $\omega_m/(2\pi) = 13.6$ kHz] is cooled to essentially zero radius and is hence not an issue. The rapid cyclotron motion, also perpendicular to the magnetic field direction, is at frequency $\omega_c'/(2\pi) = 148$ GHz. The axial motion, parallel to the magnetic field direction, is at frequency $\omega_z/(2\pi) = 63.4$ MHz.

We focus on the axial motion of a single trapped electron for the rest of this section and the following section. The common way to monitor this motion is to drive one end cap near resonance at $\omega_d \approx \omega_z$ and detect the response voltage induced across the resistor R in a tuned circuit connected to the other end cap, as shown in Fig. 2. (We do not discuss a frequency modulation which is important for practical reasons but does not change the basic idea [1].) The measured points in Fig. 3(a) fit the expected Lorentzian line shape with a width of 12.2 Hz. The width is due to damping of the particle's energy in the detection resistor R. The magnified residuals below in Fig. 3(b) clearly show that on resonance
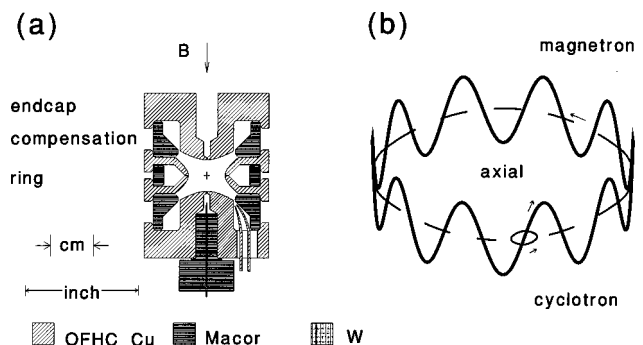

FIG. 1. Orthogonalized, hyperbolic Penning trap (a) and motion of one electron in a Penning trap (not to scale) (b).

*Present address: Dept. of Nucl. Eng., MIT, 150 Albany Street, Cambridge, MA 02139.

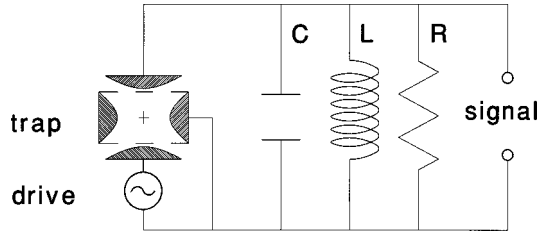†Present address: Los Alamos National Laboratory, MS H803, Los Alamos, NM 87545.

FIG. 2. Schematic of drive and detection of electron's axial motion.

FIG. 4. Undriven (except by Johnson noise) electron shorts the Johnson noise from the 4.2 K resistor at frequencies near its axial resonance.

the electron ''shorts out'' the 4.2 K Johnson noise from the resistor. Figure 4 illustrates that it is also possible to detect a single electron without the external drive. The Johnson noise from the resistor is detected (the noise spectrum is not flat because of the passband of a crystal filter) and the dip demonstrates again the ''shorting'' of this noise by the trapped electron. The width of 8.9 Hz differs slightly from that of the driven resonance in Fig. 2 which was taken at a different time, illustrating the small (but slow) variations in the effective resistance of the tuned circuit. Such a dip is a common way to observe many trapped particles, but a very well-tuned trap and optimized electronics are needed to see a single trapped particle in this way. Figure 4 requires several minutes of averaging. The advantage is that an electron which is driven only by noise stays closer to the center of the trap where the electrostatic and magnetic field are most carefully controlled.

This paper demonstrates parametric resonance as a third way to detect the axial motion of a single trapped electron. (Detailed studies of the parametric resonance of many trapped electrons have been carried out [10,11].) Before the electron's axial motion is excited it experiences only a drive so far off the 12.2 Hz wide resonance, at $\omega_d/(2\pi)$ $\approx 2\omega_z/(2\pi) \approx 127$ MHz, that its oscillation amplitude does not increase because of the drive. In this sense, the

electron remains ''in the dark,'' because the drive does not make the electron oscillate farther from the center of the trap. However, when the electron does come into parametric resonance, a large and easily observed axial oscillation at $\omega_d/2$ $\approx \omega_z$ is produced. In Sec. IV for example, we shift the electron's axial motion into parametric resonance with the drive using a cyclotron excitation, and measure how quickly a response occurs. The electron thus remains ''in the dark'' until there is a large parametric response.

The setup in Fig. 2 can produce a modulation of the trapping potential at $\omega_d \approx 2\omega_z$ instead of the direct drive mentioned previously. Such a parametric drive at frequency $\omega_d = 2(\omega_z + \epsilon)$ excites an electron oscillation at frequency $\omega_d/2 = \omega_z + \epsilon$. The one-electron, parametric oscillator has the equation of motion

$$\ddot{Z} + \gamma_z \dot{Z} + \omega_z^2 [1 + h \cos \omega_d t]Z + \lambda_4 \omega_z^2 Z^3 + \lambda_6 \omega_z^2 Z^5 = 0,$$
(1)

where Z is a dimensionless axial coordinate scaled by the trap size d [1]. The damping, at rate $\gamma_z^{-1} = 13$ ms, is due to energy dissipated in the detection resistor. Adjusting the compensation potential changes the coefficients λ_4 and λ_6 of the nonlinear terms. In terms of the Legendre expansion coefficients often used to describe Penning traps [1], $\lambda_4 = 2C_4/(1+C_2)$ and $\lambda_6 = 3C_6/(1+C_2)$.

If we start with no axial excitation ($Z \approx 0$), the nonlinear terms are not important, and the equation of motion is simply the familiar Mathieu equation with damping. Figure 5 represents the well-known properties of the Mathieu equation. For a parametric drive at $2(\omega_z + \epsilon)$, no excitation occurs until h is increased beyond a threshold. For h above this threshold
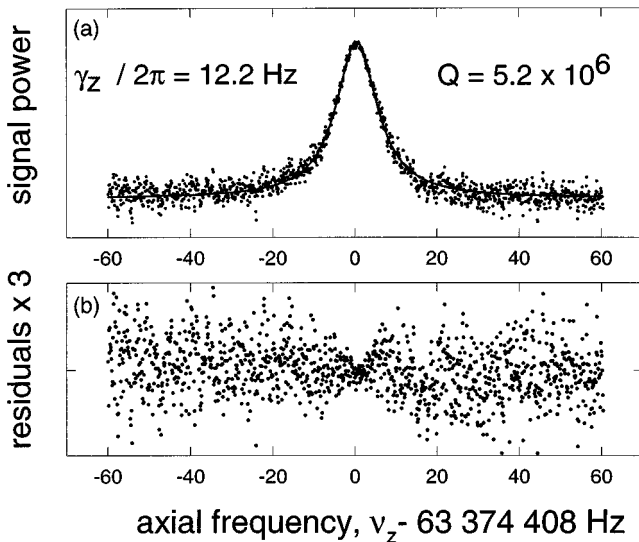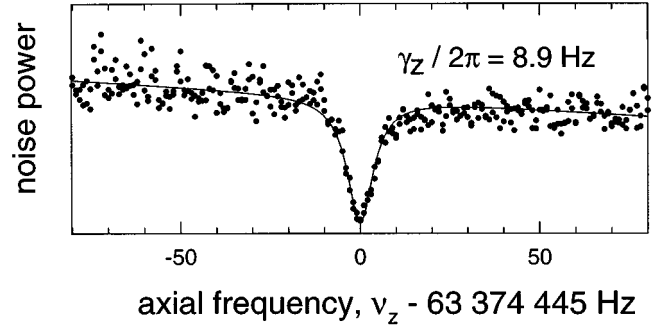

FIG. 3. (a) Response of an electron driven near its axial frequency (points) and a fit (solid curve) to the expected Lorentzian line shape. (b) Residuals show clearly the effect of ''noise shorting'' on resonance.
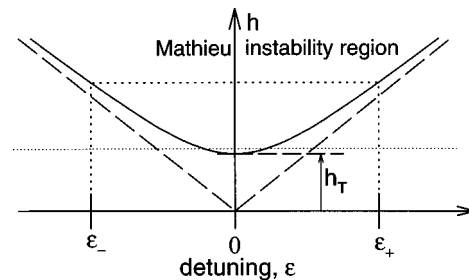

FIG. 5. Excitation range $\epsilon_+ - \epsilon_-$ vs parametric drive strength h for the Mathieu equation with damping.
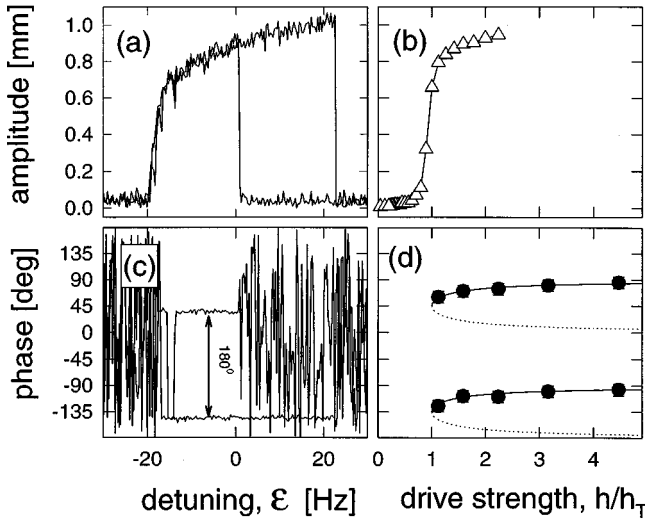
FIG. 6. Measured amplitude (a) and phase (c) of the parametric response at $\omega_d/2 = \omega_z + \epsilon$ as the frequency of the parametric drive at ω_d is swept through resonance. The phase takes one of two bistable values near resonance and is not well defined off resonance where the response amplitude is very small, as is also illustrated in the measured phase-space plot shown in Fig. 7. The amplitude threshold (b) and phase (d) of the parametric response at $\omega_d/2 \approx \omega_z$ (points) are measured as a function of the strength h of the drive. The phase plot (d) is shown superimposed on the theoretical prediction of Eq. (7).

the drive overcomes the axial damping and the excitation grows exponentially. For a parametric drive resonant at $\omega_d = 2\omega_z$ (i.e., $\epsilon = 0$), this threshold occurs at drive strength $h = h_T$ with

$$h_T = 2\gamma_z/\omega_z = 3.8 \times 10^{-7}. \tag{2}$$

(The number to the right is twice the ratio of the measured damping rate γ_z and the measured frequency ω_z.) Figure 6(b) illustrates this resonant threshold.

For a fixed drive strength $h > h_T$, Fig. 6(a) shows that parametric excitations occur for drives not exactly on resonance (i.e., $\epsilon \neq 0$) (see also Fig. 7). Excitations begin in a range $\epsilon_- < \epsilon < \epsilon_+$ with sharply defined boundaries
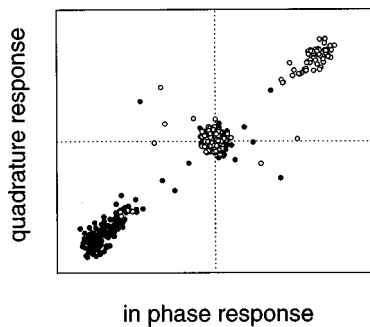

FIG. 7. Phase-space plot showing two families of attractors 180° apart as the drive frequency is being swept as in Fig. 6. Open and dark circles correspond to two different phase branches. The points clustered near the center occur primarily for an off-resonant drive.
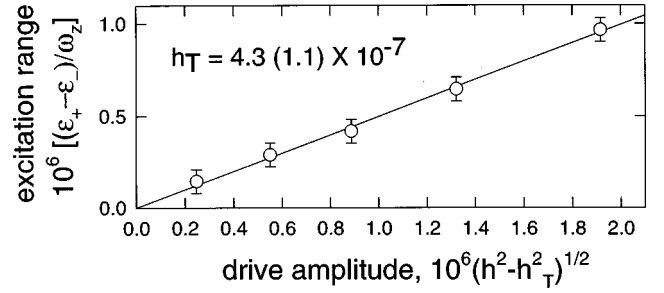

FIG. 8. Measured excitation range $\epsilon_+ - \epsilon_-$ vs parametric drive amplitude. This gives $h_T = 4.3(\pm 1.1) \times 10^{-7}$.

$$\epsilon_\pm = \pm \frac{1}{4}\omega_z\sqrt{h^2 - h_T^2}. \tag{3}$$

This well-defined excitation band is also a property of the Mathieu equation. Figure 5 represents fixed drive strength $h > h_T$ as a horizontal dotted line. The system is in the instability region from detunings between ϵ_- and ϵ_+. Figure 8 shows the measured excitation range (points) as a function of the drive strength, fit to Eq. (3) (line). From this fit we obtain $h_T = 4.3 \ (\pm 1.1) \times 10^{-7}$, in good agreement with Eq. (2).

As the excitation grows, the Mathieu equation ceases to be a valid description. The nonlinear terms [in Eq. (1)] restrict further growth until a steady state is reached. We can solve the full equation of motion given in Eq. (1) in order to obtain expressions for steady state motion. To first order in the drive strength h, the axial response is at half the drive frequency; so we let

$$Z(t) = A(t)\cos[(\omega_z + \epsilon)t + \Psi(t)]. \tag{4}$$

The amplitude $A(t)$ and the phase $\Psi(t)$ are taken to be slowly varying functions of time so that deviations from steady state can be discussed in the next section. Then, using $\epsilon \ll \omega_z$ and $\gamma_z \ll \omega_z$, the solution is a pair of coupled differential equations in A and Ψ,

$$\frac{d}{dt}A = -\frac{\gamma_z}{2}A\left[1 - \frac{h}{h_T}\sin(2\Psi)\right], \tag{5}$$

$$\frac{d}{dt}\Psi = -\epsilon + \frac{1}{4}h\omega_z\cos(2\Psi) + \frac{3}{8}\lambda_4\omega_z A^2 + \frac{5}{16}\lambda_6\omega_z A^4. \tag{6}$$

The steady state amplitudes and phases can be obtained by setting the time derivatives equal to zero. Figure 6(d) compares the measured steady state phases (points) and the calculated steady state phases (curve) obtained from Eq. (5):

$$\sin(2\Psi_{ss}) = h_T/h, \tag{7}$$

where Ψ_{ss} is the phase difference between the response and the drive for a steady state excitation. Because the driving period is half the response period, the two solutions differ in phase by 180°. This can be seen already in Eq. (1) which is invariant under a transformation $Z \to -Z$.

Figure 6(c) shows the steady state phase response as the parametric drive is swept in frequency with an amplitude response shown in Fig. 6(a). The phase is not well defined until the axial motion is excited to a nonzero amplitude near
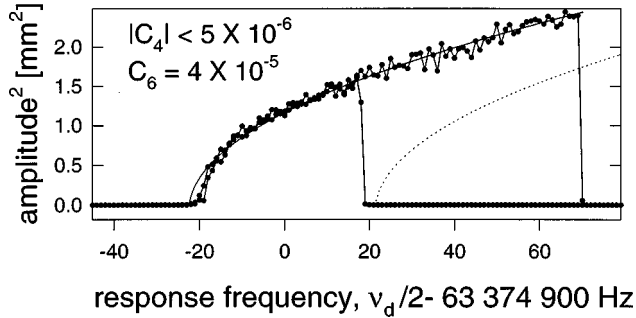
FIG. 9. Amplitude squared of the parametric response at $\omega_d/2 = \omega_z + \epsilon$ as the frequency of the parametric drive at ω_d is swept through resonance, when the trap is tuned to make C_4 as small as possible. The data are fit to parallel parabolas given by Eq. (8). (Calibration of the mm scale depends on a calculated parameter $D_6/D_4 = -0.19$ defined in Ref. [1].)

resonance. Near resonance, either of the two phases separated by 180° is equally likely. One example of each phase is superimposed in the figure, and the amplitude and phase of all measured points are also displayed in a polar, phase space plot in Fig. 7. Note that Figs. 6(a) and 6(b) correspond respectively to horizontal and vertical slices through Fig. 5.

The measured line shapes exhibit bistability and hysteresis as illustrated in Fig. 9 where the line shape extends further when the drive is swept upward in frequency than when it is swept downward. The response in the double-valued bistable region thus depends on the excitation history. In the following sections we will illustrate how to use the bistability and hysteresis to record information about an excitation made "in the dark." The trap was tuned in this case to make λ_4 as small as possible and the observed shape is determined by the value of λ_6. If the trap is deliberately mistuned to make λ_4 much larger, the excited line shape then becomes a straight line. If the trap is instead tuned so that both λ_4 and λ_6 are important, then a more complicated line shape results, one example of which is shown in Fig. 10.

All these features can be explained from the steady state solutions to the equations of motion, Eqs. (5) and (6). For parametric drives swept upward and downward through resonance, the solutions of these equations indicate that the squares of the measured amplitudes $A_\pm^2$ either vanish or lie on parallel parabolas,
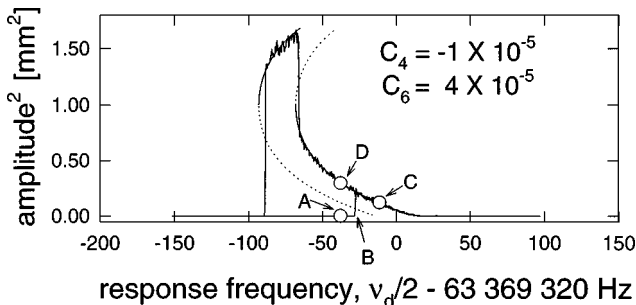

FIG. 10. Amplitude squared of the parametric response at $\omega_d/2 = \omega_z + \epsilon$ as the frequency of the parametric drive at ω_d is swept through resonance, when the trap is mistuned to increase C_4. The data are fit to parallel parabolas given by Eq. 8. (Calibration of the mm scale depends on a calculated parameter $D_6/D_4 = -0.19$ defined in Ref. [1].)
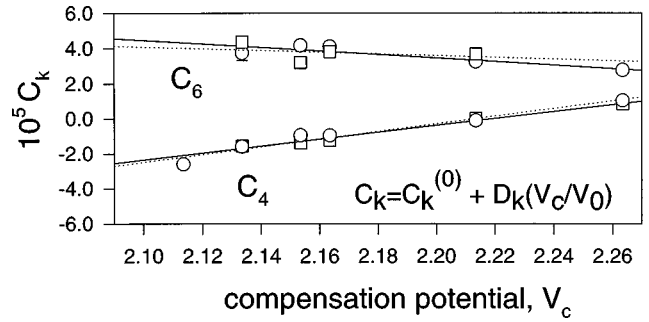

FIG. 11. Anharmonicity coefficients C_4 and C_6 as a function of compensation potential V_c. The slopes of the lines give the D_k coefficients. The dotted line is a fit to points (squares) measured for drive strength of $h/h_T = 2.2$; the solid line is a fit to points (circles) measured for drive strength of $h/h_T = 3.2$. The calculated parameter $D_6/D_4 = -0.19$ defined in Ref. [1] is assumed.

$$\frac{5\lambda_6\omega_z}{16}A_\pm^4 + \frac{3\lambda_4\omega_z}{8}A_\pm^2 + \epsilon_\pm - \epsilon = 0, \quad (8)$$

as can be seen by substituting Eqs. (3) and (7) into Eq. (6) with $\Psi = 0$. The $\pm$ in $A_\pm^2$ and $\epsilon_\pm$ corresponds to the sign of $\cos(2\Psi_{ss})$, where

$$\cos(2\Psi_{ss}) = \pm\sqrt{1 - \sin^2(2\Psi_{ss})}. \quad (9)$$

The stability of these two branches will be discussed in the next section.

Fitting the observed parametric line shapes to parallel parabolas makes it possible to determine the anharmonicity coefficients C_4 and C_6 (or equivalently λ_4 and λ_6), as well as to calibrate the dimensionless amplitude A (scaled by d). The amplitude A is related to the detected signal voltage S and trap dimension d by a constant β with $S = \beta A d$. To find this constant, a family of curves taken for different compensation potentials was fit to Eq. (8). Since the anharmonicity coefficients C_4 and C_6 vary linearly with the ratio of the compensation potential V_c and trapping potential V_0,

$$C_k = C_k^{(0)} + D_k\left(\frac{V_c}{V_0}\right), \quad (10)$$

the quadratic (a) and linear (b) coefficients from the fits depend on V_c. The ratio of the variation of a and b with respect to the compensation potential is related to β,

$$\beta = \frac{1}{d}\sqrt{\left|\frac{\Delta b/\Delta V_c}{\Delta a/\Delta V_c}\right|\frac{5}{4}\frac{D_6}{D_4}} = 0.48 \text{ V/mm.} \quad (11)$$

This depends on the well-known calculated ratio D_4/D_6. Once β is found, the dimensionless amplitude A can be expressed in terms of the detected signal $A = S/\beta d$, and the coefficients C_4, C_6, D_4, D_6 can be obtained directly from the parabola fits. This is shown in Fig. 11. The slopes of the lines are proportional to the D_k, as can be seen from Eq. (10). The coefficients displayed in Fig. 9 and Fig. 10 differ slightly from those in Ref. [3] because these coefficients are derived from the new method outlined above.

We note that for a given drive strength, a larger amplitude of excitation can be obtained in a trap with a smaller C_6. For

the larger C_6 in our cylindrical trap, however, we believe it is still possible to reproduce similar parametric excitations. From Eq. (8) we can explicitly write the ratio of the tuned ($C_4 = 0$) amplitudes for different C_6 on resonance ($\epsilon = 0$) as

$$\left(\frac{A'}{A}\right)^4 = \frac{C_6}{C_6'}\sqrt{\frac{h'^2 - h_T^2}{h^2 - h_T^2}}. \quad (12)$$

In the cylindrical geometry trap used for plasma studies [10], $C_6 = -0.1$. In the orthogonalized hyperbolic trap discussed here, $C_6 = 4\times 10^{-5}$. To achieve the same amplitude in the cylindrical trap as in this hyperbolic trap, the drive strength h would have to be about 2000 times stronger. We have, however, observed a degraded value for C_6 in the hyperbolic trap ($C_6 = 4\times 10^{-2}$) which is similar to the value in the cylindrical trap. Compared to the original hyperbolic trap amplitude, the expected amplitude for the cylindrical trap is about $\frac{1}{7}$ and that for the degraded hyperbolic trap is about $\frac{1}{6}$ (for the same drive strengths h). We have been able to observe a one-electron parametric resonance in the degraded trap (with reduced signal-to-noise ratio). Therefore, it should be possible to see a one-electron parametric signal in the cylindrical cavity trap, with roughly the same reduced signal-to-noise ratio.

III. TIME DEPENDENCE AND STABILITY

So far we have considered only the steady state line shapes. Now we examine the time it takes to reach the steady state. This is most easily done by rewriting the amplitude and phase equations (5) and (6) in terms of the in-phase and quadrature response variables $A_I \equiv A\cos(\Psi)$ and $A_Q \equiv A\sin(\Psi)$,

$$\frac{d}{dt}A_I = \left[\epsilon + \frac{1}{4}h\omega_z - \frac{3}{8}\lambda_4\omega_z A^2 - \frac{5}{16}\lambda_6\omega_z A^4\right]A_Q - \left[\frac{\gamma_z}{2}\right]A_I \quad (13)$$

$$\frac{d}{dt}A_Q = -\left[\epsilon - \frac{1}{4}h\omega_z - \frac{3}{8}\lambda_4\omega_z A^2 - \frac{5}{16}\lambda_6\omega_z A^4\right]A_I$$
$$- \left[\frac{\gamma_z}{2}\right]A_Q, \quad (14)$$

where we have left the quantity $A_I^2 + A_Q^2$ expressed as A^2. There are two regimes in which we can obtain a closed-form solution for the time dependent response. Near zero excitation, the nonlinear terms can be ignored as before, leaving the familiar Mathieu equation with exponential solutions. Near steady state excitation, the amplitude variables can be expanded about their equilibrium values to obtain linear differential equations for the deviations from steady state.

As the axial excitation begins from zero amplitude, the amplitude initially increases exponentially with the time constant τ given (within the excitation range) by

$$\tau^{-1} = \sqrt{\epsilon_\pm^2 - \epsilon^2 + (\gamma_z/2)^2} - \gamma_z/2, \quad (15)$$

which is obtained by assuming the time dependence $e^{t/\tau}$ for A_I and A_Q, and solving Eqs. (13) and (14) with $\lambda_4 = \lambda_6 = 0$. Figure 12 illustrates how the response amplitude grows as a function of time, with $t=0$ being the time at which the
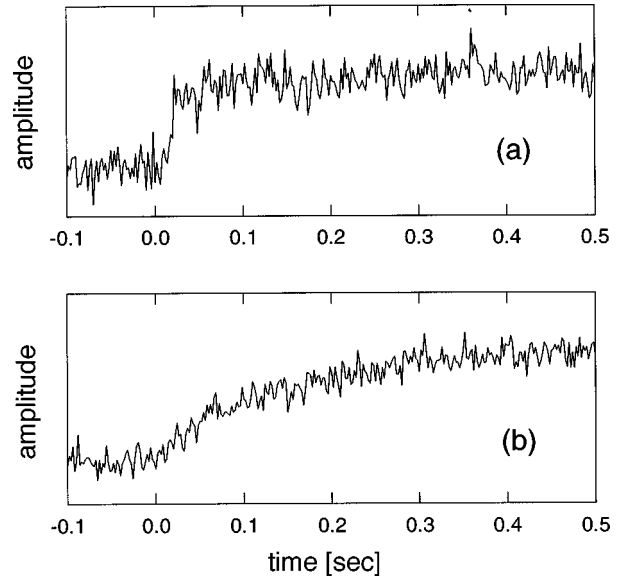

FIG. 12. Amplitude of the parametric response at $\omega_z + \epsilon$ as a function of the time after the parametric drive at $2(\omega_z + \epsilon)$ was turned on at $t=0$, for the faster resonant case of $\epsilon = 0$ in (a) and for a slower, nonresonant case of $\epsilon/(2\pi) = 20$ Hz in (b).

parametric drive is turned on. The response grows much more quickly for a resonant drive, $\epsilon = 0$ in (a), than for a nonresonant drive, $\epsilon/(2\pi) = 20$ Hz, in (b). Note from Eqs. (15) and (3) that the rise time within the excitation range can be decreased as desired by increasing the drive strength h, since $\epsilon_\pm^2$ increases with increasing h. The rise time can be increased by driving near the ends of the excitation range. Because of the exponential character of the amplitude growth, the time taken to excite to a steady state also depends in a very sensitive way upon the initial thermal excitation amplitude, suggesting excitation time measurements as a promising new way to measure axial temperature.

As the amplitude grows further, nonlinearity becomes increasingly important and eventually arrests the initial growth. The amplitude then approaches its steady state value, once again exponentially, with one of two characteristic time constants τ_1 and τ_2 given by

$$\tau_1^{-1} = \gamma_z/2 + \sqrt{(\gamma_z/2)^2 \pm 4(\partial A_\pm^2/\partial\epsilon)^{-1}|\epsilon_\pm|A_\pm^2}, \quad (16)$$

$$\tau_2^{-1} = \gamma_z/2 - \sqrt{(\gamma_z/2)^2 \pm 4(\partial A_\pm^2/\partial\epsilon)^{-1}|\epsilon_\pm|A_\pm^2}, \quad (17)$$

where $\partial A_\pm^2/\partial\epsilon$ are the slopes of the steady state response parabolas in Eq. (8). These time constants are obtained by letting $A_I = (A_I)_\pm + \Delta A_I$ and $A_Q = (A_Q)_\pm + \Delta A_Q$ where ΔA_I and ΔA_Q are small deviations from the steady state amplitudes $(A_I)_\pm$ and $(A_Q)_\pm$ with time dependence $e^{-t/\tau_{1,2}}$, and solving Eqs. (13) and (14) for $\tau_{1,2}$. Any small deviation from equilibrium can be written as a linear combination of two exponentials using the two solutions τ_1 and τ_2. The plus or minus sign in the term under the radical corresponds to the plus or minus sign in $A_\pm^2$ and will be crucial in determining which branch is stable.

Interpreting τ_1 and τ_2 as steady state approach times requires that they be positive, real quantities. If the radical term is imaginary, the electron amplitude oscillates but still
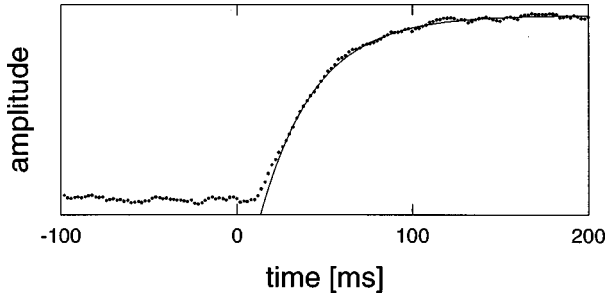
FIG. 13. Amplitude of the parametric response at $\omega_z + \epsilon$ as a function of the time after the parametric drive at $2(\omega_z + \epsilon)$ was turned on at $t=0$, where $\epsilon/(2\pi) = 15$ Hz. The solid line is a fit to an exponential with time constant $\tau = 32$ ms.

approaches equilibrium exponentially, with the single time constant $(\gamma_z/2)^{-1}$. A negative τ_2, however, leads to exponential growth of the tiniest fluctuations, rendering that branch of steady state responses unstable. Figure 13 shows an example of a typical approach to equilibrium. A 10 ms detection filter limits our ability to see the fast initial rise, but the slower approach to steady state fits well to an exponential with a time constant of 32 ms. The drive strengths, detunings, and anharmonicities are adjusted (as they usually are) so that the approach to equilibrium is oscillatory (averaged away in the data) with an overall time constant of simply $(\gamma_z/2)^{-1}$. The 32 ms approach time then results in a value of 10 Hz for $\gamma_z/2\pi$, consistent with damping rates obtained from directly measured axial linewidths as in Figs. 3 and 4.

When $\mathrm{Re}(\tau_2)$ is positive, the steady state parametric excitation is stable. This criterion is summarized in Fig. 14 which illustrates how the slopes of the parabolas for $A_\pm^2$ determine the stability of each branch. For the ''plus'' parabola to be stable, it must have a negative slope with respect to the detuning ϵ, and vice versa for the ''minus'' parabola. The slopes depend crucially on the anharmonicity coefficients. The points $\chi_\pm = -4\epsilon_\pm A_\pm^2/(\gamma_z/2)^2$ delineate the overdamped and underdamped regions. Figures 9 and 10 show
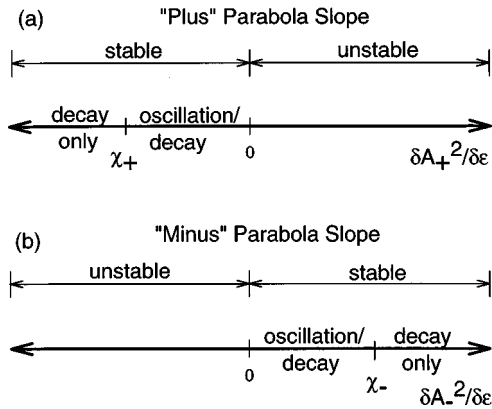

FIG. 14. Stability regions for each of the two steady state branches, as determined by τ_2 given in Eq. (17). The ''plus'' parabola [corresponding to $\cos(\Psi_{ss})$ positive] must have a negative slope to be stable [shown in (a)]. The ''minus'' parabola [corresponding to $\cos(\Psi_{ss})$ negative] must have a positive slope to be stable [shown in (b)]. The oscillatory regions, delineated by $\chi_\pm = -4\epsilon_\pm A_\pm^2/(\gamma_z/2)^2$, are discussed in the text.

measured line shapes superimposed on calculated parabolas. The solid calculated curves are stable solutions whereas the dotted curves are unstable. Not surprisingly, the experimental responses lie wholly on the stable branches. As a final check of the stability criteria, the phase of the response is measured and shown in Fig. 6(d). These points were taken with both anharmonicity coefficients λ_4 and λ_6 positive; thus both slopes were positive, forcing the ''minus'' branch to be the stable one. Again, the measured phases lie on the stable region, $\cos(2\Psi_{ss}) < 0$, shown as a solid curve.

The time dependence and stability of the system can be formulated in a more general way. This may also allow an easier treatment of other aspects of the system such as parametric feedback. We first review some of the properties of nonlinear dynamics following closely the treatment presented by [12]. Specifically, we can examine the Liapunov stability of a particular point in phase space, which is the stability of the point under perturbations in the initial conditions. Similarly, we can examine the structural stability of the whole system, which is the stability of the topology of the phase portrait under perturbations in the parameters of the differential equations describing the system.

The system can be described, in general, by n differential equations [in our case, Eqs. (5) and (6)],

$$\dot{x}_1 = F_1(x_1, x_2, \ldots, x_n),$$
$$\dot{x}_2 = F_2(x_1, x_2, \ldots, x_n),$$
$$\vdots$$
$$\dot{x}_n = F_n(x_1, x_2, \ldots, x_n), \qquad (18)$$

where $F(x)$ is a vector field. If x^s is an equilibrium point or steady state solution (now including the zero amplitude solution as well), then $F_i(x^s) = 0$ for all i. We denote the steady state solution by

$$x^s = (x_1^s, x_2^s, \ldots, x_n^s). \qquad (19)$$

We can study the stability of this point under perturbations in the initial conditions. Consider the small deviation $x \rightarrow x^s + \xi$ of the vector field equation, $\dot{x} = F(x)$. Then the time derivative of the deviation can be expanded as

$$\dot{\xi} = F(x^s + \xi) = F(x^s) + F_x(x^s)\xi + \frac{1}{2}F_{xx}(x^s)\xi^2 + \cdots$$
$$\approx F_x(x^s)\xi, \qquad (20)$$

where F_x is the Jacobian of F. For the point x^s to be (Liapunov) stable, we require that for every neighborhood N of x^s in the phase space there exist a smaller neighborhood $N_1 \subset N$ of x^s, such that every solution starting in N_1 will remain in N for all $t > 0$. If all solutions tend to x^s as $t \rightarrow \infty$, then x^s is said to be asymptotically stable. It can be shown that for asymptotic stability, $\xi \rightarrow 0$ as $t \rightarrow \infty$, which is equivalent to the condition that $\mathrm{Re}\,\lambda_i < 0$ for all eigenvalues λ_i of $K \equiv F_x(x^s)$. Note that K can be considered as a function of system parameters.

For the one-electron parametric oscillator, the system is described by the differential equations for $\dot{A}$ and $\dot{\Psi}$, given by Eqs. (5) and (6). The nonlinearity in the system is due to the
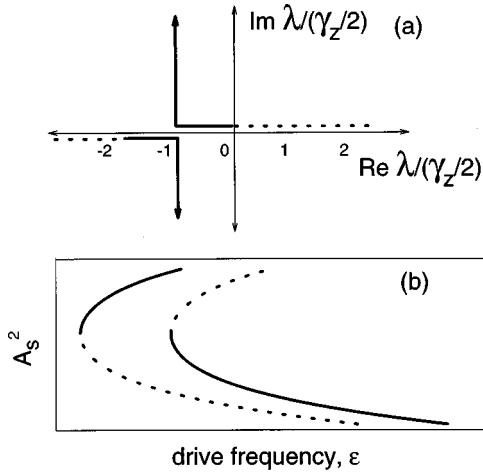
FIG. 15. Steady state branches: (a) The eigenvalues of the associated vector field K. When both eigenvalues have Re $\lambda < 0$, then the corresponding steady state solution is stable. A similar graph exists for each of the branches (''plus'' parabola and ''minus'' parabola). (b) The steady state solutions given by Eqs. (5) and (6). The solid lines are stable, whereas the dashed lines are unstable. Similar graphs exist for anharmonicities of the opposite sign.

anharmonicity, which causes the resonant frequency to depend on the excitation amplitude. This restricts the growth of the amplitude of the response, which then approaches a steady state. We quantify the anharmonicity in a term J defined by

$$J = \frac{3}{8}\lambda_4 \omega_z A^2 + \frac{5}{16}\lambda_6 \omega_z A^4. \tag{21}$$

Using J, the Jacobian for $A^s \neq 0$ is

$$K = \begin{pmatrix} 0 & 2A^s \epsilon_\pm \\ \left.\dfrac{\partial J}{\partial A}\right|_s & -\gamma_z \end{pmatrix}, \tag{22}$$

with the eigenvalues

$$\lambda_1 = (\gamma_z/2)\left(-1 - \sqrt{1 \pm A^s \left.\frac{\partial J}{\partial A}\right|_s \frac{2|\epsilon_\pm|}{(\gamma_z/2)^2}}\right) = -\tau_1^{-1}, \tag{23}$$

$$\lambda_2 = (\gamma_z/2)\left(-1 + \sqrt{1 \pm A^s \left.\frac{\partial J}{\partial A}\right|_s \frac{2|\epsilon_\pm|}{(\gamma_z/2)^2}}\right) = -\tau_2^{-1}, \tag{24}$$

where the sign under the radical depends on the sign of $\cos(2\Psi_{ss})$ as before. (Here, $\Psi^s = \Psi_{ss}$ defined earlier.) The stable steady state solutions correspond to those having Re $\lambda_i < 0$ for both eigenvalues. Figure 15 shows (a) the eigenvalues and (b) the steady state solutions. The deviations will approach or diverge from the steady state solution with exponential rates given by the real parts of the eigenvalues. The delineation points $\chi_\pm$, discussed earlier, correspond to eigenvalues leaving the real axis and occur at $(-1,0)$ in Fig. 15(a).

For the zero-amplitude solutions $A^s = 0$, the phase is not defined. We can, however, take a small nonzero A and then take the limit as $A \to 0$. The Jacobian is then

$$K \approx (-\gamma_z/2)\begin{pmatrix} 1 - \left(\dfrac{h}{h_T}\right)\sin(2\Psi^s) & 0 \\ 0 & 2\left(\dfrac{h}{h_T}\right)\sin(2\Psi^s) \end{pmatrix}, \tag{25}$$

where Ψ^s is the steady state phase for the small amplitude A. The eigenvalues are given directly by the diagonal elements. Using Eq. (6), we have, for $\sin(2\Psi^s) > 0$,

$$\lambda_A = -\gamma_z/2 + \sqrt{\epsilon_\pm^2 - \epsilon^2 + (\gamma_z/2)^2}, \tag{26}$$

$$\lambda_\Psi = -2\sqrt{\epsilon_\pm^2 - \epsilon^2 + (\gamma_z/2)^2}, \tag{27}$$

which for $|\epsilon| < |\epsilon_\pm|$ are not both < 0. Note that Eq. (7) is not applicable for this $A^s = 0$ case. The $A^s = 0$ solution is clearly unstable insofar as the amplitude diverges with an exponential time constant $(\lambda_A)^{-1} = \tau$ [the same time constant given in Eq. (15)]. For $\sin(2\Psi^s) < 0$, we have

$$\lambda_{A'} = -\gamma_z/2 - \sqrt{\epsilon_\pm^2 - \epsilon^2 + (\gamma_z/2)^2}, \tag{28}$$

$$\lambda_{\Psi'} = +2\sqrt{\epsilon_\pm^2 - \epsilon^2 + (\gamma_z/2)^2}. \tag{29}$$

The $\lambda_{A'}$ eigenvalue would lead to a reduced amplitude; however, as $\xi \to 0$, $F(x^s)$ for our small nonzero A can no longer be neglected compared to $F_x(x^s)\xi$ in Eq. (20). Therefore, $\lambda_{A'}$ and $\lambda_{\Psi'}$ are not valid solutions.

Finally, we examine the effect of perturbations on the structural stability of the system. We restrict our discussion to the behavior of the family of equilibrium points, that is, whether or not they remain stable or unstable under changes of system parameters. This is useful in determining the effect of small fluctuations or uncertainties on the robustness of an excitation of the electron. For changes in $h > h_T$ and $\gamma_z > 0$, pairs of eigenvalues, given by Eqs. (23) and (24), move toward the $(0,0)$ or $(-2,0)$ points, never crossing the imaginary axis. This is depicted in Fig. 15(a). A stable (unstable) pair of eigenvalues therefore remains stable (unstable). Thus, the system is structurally stable under changes in either $h > h_T$ or $\gamma_z > 0$. Variations in the system parameters λ_4 and λ_6 also result in migration of the eigenvalues toward or away from the $(0,0)$ or $(-2,0)$ points. Eigenvalues far away do not cross these points, and are structurally stable under small variations in λ_4 or λ_6. Eigenvalues near these points, on the other hand, may be structurally unstable. The special points $(0,0)$ and $(-2,0)$ correspond to the vertices of the parabolas given by Eq. (8) and shown in Fig. 15(b). Any family of eigenvalues of the parametric oscillator can be depicted by Fig. 15(a), except for pathological cases such as $\lambda_6 = 0$ or both $\lambda_4, \lambda_6 = 0$. In this broader sense, the various systems have topological equivalence and structural stability.

IV. CYCLOTRON MOTION COUPLED TO A CAVITY

The cyclotron oscillation frequency ω_c' is more than 2000 times higher than the axial frequency ω_z. This motion can
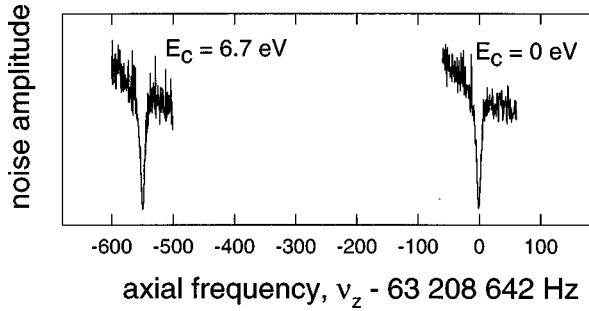
FIG. 16. Axial resonance of a single trapped electron (noise-shorting dip to the right) is shifted to a lower frequency (left) when the electron's cyclotron motion is excited to an energy of E_c =6.7 eV. When the cyclotron drive is turned off, the dip shifts back as the electron damps via its coupling to the radiation field in the trap cavity.

be excited with a very pure microwave drive [13] which enters the trap through the small tube shown in Fig. 1. A cyclotron excitation to energy E_c results in a shift in the axial frequency,

$$\frac{\Delta\omega_z}{\omega_z} = -\frac{E_c}{2mc^2}, \tag{30}$$

and a shift in the cyclotron frequency,

$$\frac{\Delta\omega_c'}{\omega_c'} = -\frac{E_c}{mc^2}. \tag{31}$$

Both of these shifts are due to special relativity and are often thought of as relativistic mass shifts since special relativity has the effect of replacing the mass m in the mass-dependent frequencies by γm, where γ is the familiar relativistic factor (the total energy, rest mass energy plus kinetic energy, divided by the rest energy).

For the purposes of this paper, a cyclotron excitation simply causes the axial frequency to shift. The dip to the right in Fig. 16 is the undriven axial resonance observed for no cyclotron excitation. A cyclotron excitation of E_c=6.7 eV causes the axial frequency to shift downward by 550 Hz (the left dip in Fig. 16). Turning off the cyclotron microwave drive causes the electron resonance dip to shift back to its original position as the cyclotron motion spontaneously emits synchrotron radiation. This spontaneous emission is modified by the presence of a surrounding microwave cavity which can either enhance or inhibit spontaneous emission [6,14,15].

For the large cyclotron excitations used here, the time it takes the axial resonance to come within a linewidth of its E_c=0 position is of order 100 ms. However, it takes several minutes of signal averaging to observe the dip in the noise resonance; it is not possible to time resolve the shifting dip. One could apply a drive directly at ω_z for E_c=0 and measure how long it takes to see the drive response illustrated in Fig. 3. Instead, we apply a parametric drive at $\omega_d=2\omega_z$ and take advantage of the large signal which is rapidly produced by a parametric excitation. At time $t=0$ the microwave drive is turned off and the cyclotron energy begins to damp. Spe-
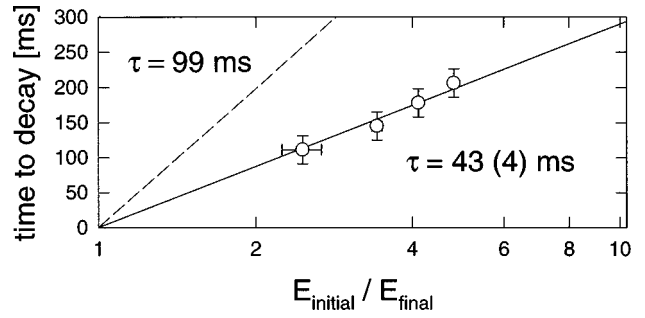

FIG. 17. Time between turning off the cyclotron drive and the first observation of a parametric axial response, as a function of the energy of the initial cyclotron excitation. The (solid) fitted line (constrained to pass through the origin) shows an exponential damping time for the cyclotron motion which is shorter than the spontaneous emission time in free space (dashed line). Spontaneous emission is enhanced by the coupling of the electron cyclotron motion and the cavity.

cial relativity shifts the axial resonance upward, eventually into parametric resonance with the drive. After a delay, a parametric response thus begins (much like those in Fig. 12). The response grows with a time constant that is due to a filter included to improve the signal-to-noise ratio. When this filter is removed we can observe rise times less than 10 ms but the signal-to-noise ratio is such that averaging over hours then becomes necessary. Figure 17 shows four measurements made of the time delay before a response is observed, for different values of the initial cyclotron excitation. Each point is an average of ten trials. The fitted line (constrained to pass through the origin) gives an exponential damping time for the cyclotron motion of 43±4 ms. In free space, this cyclotron radiation lifetime would be 99 ms, and so the spontaneous emission is clearly enhanced by the coupling between the cyclotron motion and the trap cavity. In the past, only the longer damping time for inhibited spontaneous emission could be observed [6].

During these measurements we also observed the interesting behavior of two electrons whose cyclotron motions are excited. As a context, Fig. 18 (light line) shows the axial frequency of one electron as a cyclotron drive is swept downward (large shift) and upward (small excitation) through resonance. As in earlier observations [13], the frequency of a driven and locked axial resonance is observed continuously. The characteristic, triangular resonant shape of the anharmonic oscillator is evident and this anharmonicity
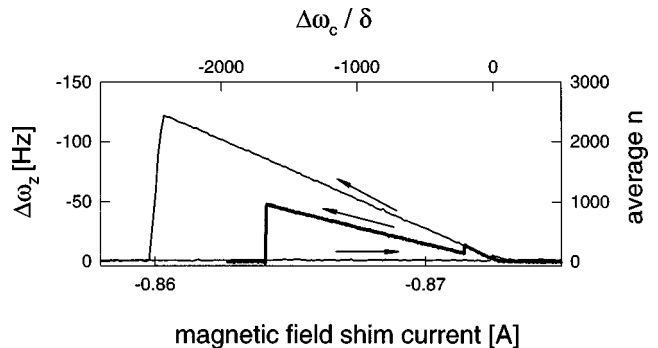

FIG. 18. Anharmonic cyclotron resonance for one (light line) and for two (bold line) electrons.

is due to special relativity as stated in Eqs. (30) and (31). Sweeping the cyclotron drive downward through resonance when two electrons are present in the trap exhibits a slightly more complicated resonance structure shown in Fig. 18 (bold line). Initially the slope is the same for two electrons as for one. This occurs because the center-of-mass motion is observed and the center of mass of two electrons has the same charge-to-mass ratio as does one electron. The cyclotron excitation energy drops suddenly but not to zero, presumably because one electron remains excited while the second damps to the center of the trap. The excitation of the excited electron continues and increases as the drive is swept downward in frequency until eventually this excitation also drops out. The measured ratio of the two slopes is 1.9 ± 0.2. Related couplings of two antiprotons in cyclotron orbits with frequencies shifted by special relativity have been observed [16], as have similar couplings between a simultaneously trapped antiproton and H^- ion.

The basic features of the two electron resonance can be explained by a simple model of two oscillators coupled by a force F. The equations of motion are

$$m_1 \ddot{z}_1 = -kz_1 + F_{21} - \gamma_z(\dot{z}_1 + \dot{z}_2), \qquad (32)$$

$$m_2 \ddot{z}_2 = -kz_2 + F_{12} - \gamma_z(\dot{z}_1 + \dot{z}_2), \qquad (33)$$

where z_1, z_2 are the displacements from equilibrium, and F_{21} is the force of particle 2 on particle 1. We add and subtract the equations to get the behavior of the normal mode motions, a center-of-mass motion, and a breathing motion. The center of charge rather than the center of mass is actually detected. However, since $\gamma = \sqrt{1 - (v/c)^2} \approx 1$, these are about the same. Then we have

$$\begin{pmatrix} z_+ \\ z_- \end{pmatrix} = \frac{1}{2} \begin{pmatrix} z_1 + z_2 \\ z_1 - z_2 \end{pmatrix}. \qquad (34)$$

We take $\ddot{z}_1 \approx \ddot{z}_2 \approx \ddot{z}_+$, motivated by a rigid body approximation. The equation of motion for the center-of-charge mode is, then,

$$\frac{(m_1 + m_2)}{2} \ddot{z}_+ = -kz_+ - 2\gamma_z \dot{z}_+. \qquad (35)$$

Thus, the signal due to the center of charge is the familiar Lorentzian at a frequency

$$\omega_{z,+} = \sqrt{k \Big/ \frac{(m_1 + m_2)}{2}}. \qquad (36)$$

Consider the case where the cyclotron motions of both electrons are excited. Then $m_1 = m_2 = \gamma m$, and

$$\omega_{z,+} = \sqrt{k/\gamma m}. \qquad (37)$$

The variation in the axial frequency with respect to γ is $\Delta \omega_{z,+}/\omega_{z,+} = -\frac{1}{2}\Delta\gamma/\gamma$. The variation of the cyclotron frequency, is $\Delta\omega_c'/\omega_c' = -\Delta\gamma/\gamma$. This gives

$$\frac{\Delta\omega_{z,+}}{\omega_{z,+}} = \frac{1}{2}\frac{\Delta\omega_c'}{\omega_c'}, \qquad (38)$$

which has the same slope as for one particle. If, on the other hand, one electron is deexcited and the other is excited, $m_1 = m$ and $m_2 = \gamma m$. Then, the frequency of oscillation is

$$\omega_{z,+} = \sqrt{k \Big/ \frac{(1+\gamma)m}{2}}. \qquad (39)$$

The variation in the axial frequency with respect to γ is $\Delta\omega_{z,+}/\omega_{z,+} = -\frac{1}{4}[2\gamma/(1+\gamma)]\Delta\gamma/\gamma$. The variation of the cyclotron frequency remains $\Delta\omega_c'/\omega_c' = -\Delta\gamma/\gamma$. This gives (since $\gamma \approx 1$)

$$\frac{\Delta\omega_{z,+}}{\omega_{z,+}} = \frac{1}{4}\frac{\Delta\omega_c'}{\omega_c'}, \qquad (40)$$

which is one-half that for one particle. In this model, it is clear that when the system drops from the first branch to the second branch, the axial shift will be divided by 2. This can be seen in Fig. 18. We check that our initial assumption $\ddot{z}_1 \approx \ddot{z}_2 \approx \ddot{z}_+$ is valid by recognizing that on the second branch the axial driving force will be halfway between the two natural frequencies.

V. MEASURING THE CYCLOTRON FREQUENCY "IN THE DARK"

The measured enhanced spontaneous emission rate reported in the previous section was done "in the dark" insofar as the cyclotron decay occurred in the absence of any drive able to make an appreciable increase in the electron's excitation amplitude. However, the field-effect transistor (FET) amplifier which detected the voltage induced across the resistor was left on continuously and energy dissipated in this FET caused the effective temperature of the resistor R to be greater than the ambient 4.2 K. We now consider a cyclotron frequency measurement which is more "in the dark" insofar as the FET detection amplifier is turned off during the crucial part of the measurement, allowing the resistor temperature to decrease to the ambient 4.2 K. The parametric axial oscillator is used as a 1-bit memory to record whether or not a cyclotron excitation occurred. Since special relativity produces a shift in the electron's axial frequency when the cyclotron motion is excited, we need only detect a shift in the axial frequency. A parametric drive is turned on at a frequency corresponding to point A in Fig. 10. The axial motion of the electron is not excited. A downward, relativistic shift in the electron's axial frequency is equivalent to shifting the frequency of the parametric drive upward to point C in the figure. The electron's axial motion remains unexcited during the initial (and critical) cyclotron excitation, until the electron enters the single valued region at arrow B enroute to point C. Even when the axial frequency shifts back because the cyclotron drive is turned off, the parametric hysteresis makes the axial excitation persist as indicated by point D in the figure. The FET detector is subsequently turned on to read out the 1-bit memory, to find out whether an axial frequency shift (and hence a cyclotron excitation) took place.

The energy levels for the lowest cyclotron eigenstates (number states) are shown in Fig. 19(a). Since no spin is
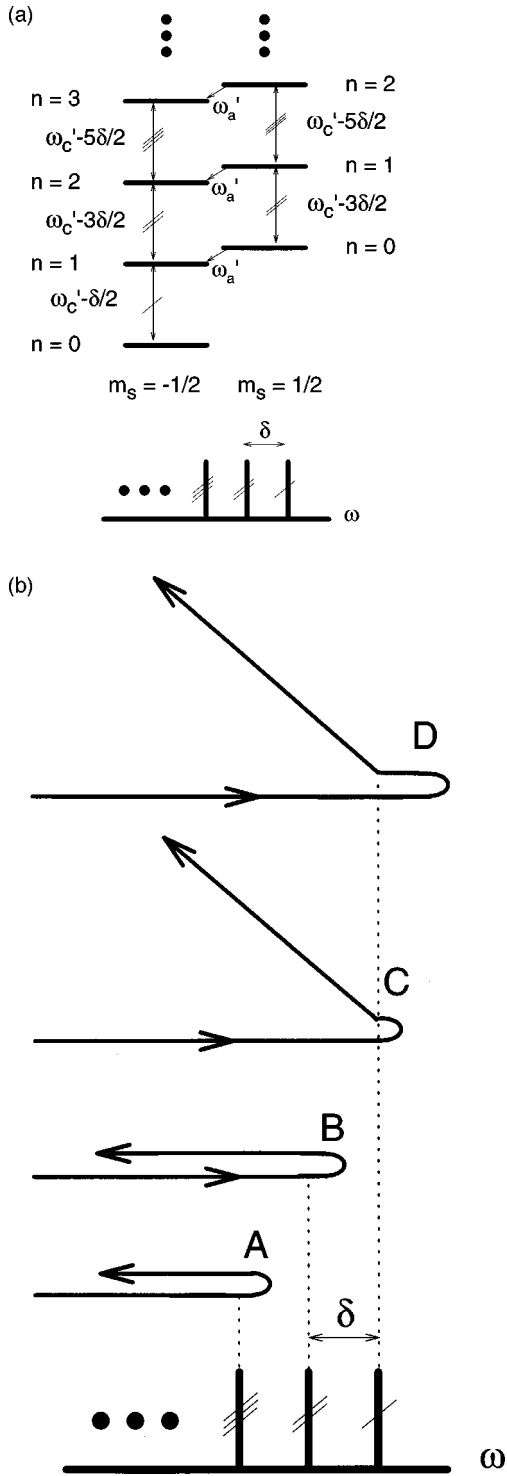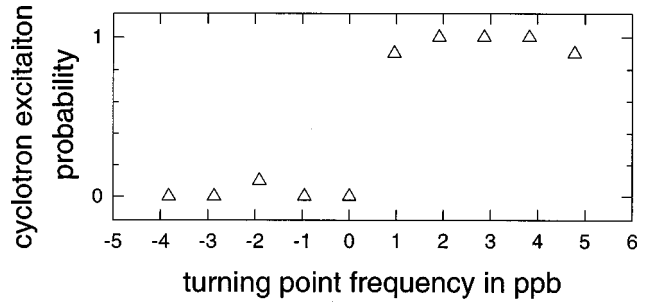
(a)

FIG. 20. Probability for ''pulled'' relativistic excitation of the cyclotron motion of one electron as a function of the turning point frequency from which the cyclotron drive is swept to lower frequencies.

quency between successively higher pairs of energy levels is lower by

$$\delta = \frac{\hbar(\omega_c')^2}{mc^2}, \qquad (41)$$

where $\delta/\omega_c' = 10^{-9}$. To make a cyclotron excitation, a cyclotron drive frequency is swept upward to a turning point and then back downward [13,17], as illustrated in Fig. 19(b). If the turning point is higher in frequency than the unshifted cyclotron frequency [C and D in Fig. 19(b)], a large excitation is expected (like that directly detected with the FET turned on, in Fig. 18). If the turning point is less than the unshifted cyclotron frequency (and there is no power broadening), then no excitation is expected [A and B in Fig. 19(b)]. Figure 20 shows the probability of observing a large excitation as a function of turning point frequencies which are separated from each other by 1 part in 10^9 (1 ppb). Each point is the average of ten trials. It took 2 h to produce this curve owing largely to the time required to turn on and off the heavily filtered voltage supply for the FET. The observed edge is very clean and has a resolution width less than 1 ppb. This is gratifying insofar as 1 ppb corresponds to the relativistic frequency shift due to a single quantum excitation of the cyclotron oscillator. We have thus succeeded in resolving a one quantum excitation of the cyclotron motion using special relativity, without resorting to any magnetic field inhomogeneities which couple the various electron motions and severely broaden the resonance lineshapes [7,18]. This resolution also indicates that the magnetic field produced by a self-shielding, superconducting solenoid [19,20] drifted less than 1 ppb during this particular 2-h measurement.

For a completely ''in the dark'' experiment, the axial motion must also be decoupled from the thermal noise from the detection resistor. This is easily accomplished by detuning the trap potential to make the axial frequency no longer resonant with the LCR circuit shown in Fig. 2. However, the axial excitation will remain at the average energy corresponding to 4.2 K insofar as such detuning also eliminates the axial damping. To cool the axial motion below 4.2 K, it should be possible to employ cavity sideband cooling [21]. At the 4.2 K ambient temperature of our current traps, the cooling limit for the axial motion would be 2 mK. Electrons recently confined at 50 mK [22] could, however, be cooled to μK axial temperatures.

(b)

FIG. 19. (a) Energy eigenstates (number states) for the relativistic electron cyclotron oscillator, with cyclotron quantum number n and spin quantum number m_s. (b) Representation of the change in the frequency of the drive applied to excite the cyclotron motion of an electron (above) in comparison to the resonant frequencies (below). For a cyclotron motion initially in its ground state, sweeping the drive to the ''turning points'' A or B ideally produces no excitation, whereas sweeping to the turning points C or D allows a large excitation.

flipped, we focus on one of the two ''ladders'' of Landau levels. Because of special relativity, the cyclotron energy levels are not equally spaced. Instead, the transition fre-

VI. CONCLUSION

We look forward to repeating these studies in a cylindrical Penning trap [23], where the radiation modes are now well measured and understood [10,11,24]. The ''in the dark'' techniques demonstrated here, together with the desirable properties of the cylindrical Penning trap, suggest the likelihood of a new generation of measurements of the electron's magnetic moment with higher accuracy and smaller systematic error. The increased understanding of the time dependence and stability of parametric excitations should permit the faster cyclotron frequency detection necessary for an improved magnetic moment measurement [25]. This understanding may also permit investigations of self-excitation using parametric feedback, as well as *in situ* electron

temperature measurements. Observing a clean parametric resonance with a single electron also demonstrates the sensitivity required to study the nonlinear dynamics of two, three, four, and more interacting electrons. An initial study of the collective plasma behavior of many trapped electrons has been carried out [10,11], and now it should be possible to study the onset of collective motions as the particle number is increased from unity.

[1] L.S. Brown and G. Gabrielse, Rev. Mod. Phys. **58**, 233 (1986).

[2] L.D. Landau and E.M. Lifshitz, *Mechanics* (Pergamon Press, New York, 1976).

[3] C.H. Tseng and G. Gabrielse, Appl. Phys. B: Lasers Opt. **60**, 95 (1995).

[4] G. Gabrielse, X. Fei, L.A. Orozco, R.L. Tjoelker, J. Haas, H. Kalinowsky, T.A. Trainor, and W. Kells, Phys. Rev. Lett. **65**, 1317 (1990).

[5] D. Wineland, P. Ekstrom, and H.G. Dehmelt, Phys. Rev. Lett. **31**, 1279 (1973).

[6] G. Gabrielse and H.G. Dehmelt, Phys. Rev. Lett. **55**, 67 (1985).

[7] R.S. VanDyck, Jr., P.B. Schwinberg, and H.G. Dehmelt, Phys. Rev. Lett. **59**, 26 (1987).

[8] T. Kinoshita, Rep. Prog. Phys. **59**, 1459 (1996).

[9] G. Gabrielse, Phys. Rev. A **27**, 2277 (1983).

[10] J. Tan and G. Gabrielse, Phys. Rev. Lett. **67**, 3090 (1991).

[11] J. Tan and G. Gabrielse, Phys. Rev. A **48**, 3105 (1993).

[12] J.M.T. Thompson and H.B. Stewart, *Nonlinear Dynamics And Chaos* (John Wiley and Sons, New York, 1986).

[13] G. Gabrielse, H.G. Dehmelt, and W. Kells, Phys. Rev. Lett. **54**, 537 (1985).

[14] L.S. Brown, G. Gabrielse, K. Helmerson, and J. Tan, Phys. Rev. Lett. **55**, 44 (1985).

[15] L.S. Brown, G. Gabrielse, K. Helmerson, and J. Tan, Phys. Rev. A **32**, 3204 (1985).

[16] G. Gabrielse, J. Gröbner, W. Jhe, H. Kalinowsky, D. Phillips, and W. Quint, Nucl. Phys. A **558**, 701 (1993).

[17] H. Dehmelt, Ann. Phys. (Paris) **10**, 777 (1985).

[18] R. Mittleman, F. Palmer, G. Gabrielse, and H.G. Dehmelt, Proc. Natl. Acad. Sci. USA **88**, 9436 (1991).

[19] G. Gabrielse and J. Tan, J. Appl. Phys. **63**, 5143 (1988).

[20] G. Gabrielse, J. Tan, P. Clateman, L.A. Orozco, S.L. Rolston, C.H. Tseng, and R. Tjoelker, J. Magn. Reson. **91**, 564 (1991).

[21] G. Gabrielse, *Laser Manipulation of Atoms and Ions*, edited by E. Arimondo, W.D. Phillips, and F. Strumia (North-Holland, New York, 1992).

[22] S. Peil and G. Gabrielse (unpublished).

[23] J. Tan and G. Gabrielse, Appl. Phys. Lett. **55**, 2144 (1989).

[24] G. Gabrielse and J. Tan, *Cavity Quantum Electrodynamics*, edited by P.R. Berman (Academic, New York, 1994).

[25] D. Enzer and G. Gabrielse, Phys. Rev. Lett. **78**, 1211 (1997).